Model-supported characterization of a PEM water electrolysis cell for the effect of compression

Frensch, Steffen Henrik; Olesen, Anders Christian; Simon Araya, Samuel; Kær, Søren Knudsen

Published in:
Electrochimica Acta

DOI (link to publication from Publisher):
10.1016/j.electacta.2018.01.040

Publication date:
2018

Document Version
Early version, also known as pre-print

Model-supported characterization of a PEM water electrolysis cell for the effect of compression

Steffen Henrik Frensch[a,*], Anders Christian Olesen[a], Samuel Simon Araya[a], Søren Knudsen Kær[a]

[a]*Aalborg University, Department of Energy Technology, Pontoppidanstræde 111, 9220 Aalborg Øst, Denmark*

Abstract

This paper investigates the influence of the cell compression of a PEM water electrolysis cell. A small single cell is therefore electrochemically analyzed by means of polarization behavior and impedance spectroscopy throughout a range of currents (0.01 A cm^{-2} to 2.0 A cm^{-2}) at two temperatures (60 °C and 80 °C) and eight compressions (0.77 MPa to 3.45 MPa). Additionally, a computational model is utilized to support the analysis. The main findings are that cell compression has a positive effect on overall cell performance due to decreased contact resistances, but is subject to optimization. In this case, no signs of severe mass transport problems due to crushed transport layers are visible in either polarization curves or impedance plots, even at high currents. However, a Tafel plot analysis revealed more than one slope throughout the current range. The change in the Tafel slope is therefore discussed and connected to the electrochemical reaction or an ohmic contribution from a non-electrode component.

Keywords: PEM water electrolysis, Impedance spectroscopy, Contact resistance, Model validation, Clamping pressure

1. Introduction

Energy storage is considered crucial for a successful transition to carbon neutral energy production. A hydrogen based energy production can be a key technology as hydrogen can be stored and distributed as a liquid or gas, and utilized in fuel cells (FC) to produce electrical energy and heat [1]. Nowadays, the main source of hydrogen is from steam reformed hydrocarbons or alcohols [2] with inevitable release of greenhouse gases. However, hydrogen can also be produced through water electrolysis (WE), where water is electrochemically split into its elements, hydrogen and oxygen. If the required electrical energy comes from renewable energy sources, this process can be considered CO_2 neutral. Additionally, electrolyzers can potentially provide grid-services for frequency stability [3].

Polymer electrolyte membrane (PEM) electrolysis can be considered an evolving technology that is entering the market and has attracted more research interest in the past few years due to certain advantages [2, 4]. Among others, PEM electrolyzers can be manufactured in compact systems due to their solid electrolyte membrane with small footprints and offer relatively high efficiency. In the context of grid stability, they are especially interesting due to good dynamic response times and start/stop behavior, and a wide operating range [5]. Comparably fast starts are possible due to the operation at low temperatures of around 60 °C to 100 °C. Furthermore, the hydrogen gas purity can be maintained fairly high at 99.999% which makes further purification redundant [6]. PEM electrolyzers offer the possibility to operate under high pressures which allows hydrogen gas production at more than 100 bar [7]. Depending on the application, internal pressurization may make external gas compressors redundant and therefore reduce system complexity and cost [8]. Pure oxygen as a byproduct might be utilized and monetized in PEM FC or other applications, or released to the atmosphere [9]. The major drawback is the high cost due to the need of precious materials. Additionally, acceptable lifetime under dynamic operation has yet to be proven [5].

An improvement in performance and durability requires proper characterization methods. Besides classic polarization curves (IV), other tools that researchers employed on WE include current interrupt, cyclic

*Corresponding author

Email addresses: stf@et.aau.dk (Steffen Henrik Frensch), aco@et.aau.dk (Anders Christian Olesen), ssa@et.aau.dk (Samuel Simon Araya), skk@et.aau.dk (Søren Knudsen Kær)

voltammetry, more visual approaches, such as electron microscopy, and electrochemical impedance spectroscopy (EIS) [10, 11]. EIS is a versatile characterization technique that is already widely used in fuel cell applications [12, 13] and many researchers have also implemented EIS as a tool in their investigations on PEM electrolyzers [14, 15]. With the above mentioned characterization techniques, performance investigations for different membrane-electrode-assemblies (MEAs) in terms of materials and loading were compared [16, 17], as well as studies on the impact of the feed water flow type [18] and stoichiometry [19].

However, not many systematic studies are available in the literature that reveal more insight about how various operation conditions affect cell performance. Moreover, with the design consisting of multiple solid layers clamped between two end plates, the compression pressure is an interesting parameter and possibly subject to optimization. While the compression pressure is reasonably well researched for FC, WE lacks studies [20, 5]. EIS can provide useful insights for analyzing compression [21, 22].

This paper investigates the performance of a single cell under different current and temperature operation points at various compressions. The purpose is to better understand what the most relevant operation parameters are. The experimental work is supported by computational modelling in order to extract characteristic parameters such as the exchange current density. The combination of experimental data and a model approach also helps to divide the different resistance contributions between the components.

2. Methodology

All experiments are carried out on a single cell setup. Custom made MEAs by EWII Fuel Cells A/S (Denmark) with an active area of 2.89 cm^2 (1.7 cm*1.7 cm) are tested. The assembly consists of a commercial Nafion 117 membrane coated with Iridium oxide (IrO_2, 0.3 $mg\,cm^{-2}$) on the anode and carbon-supported Platinum (Pt/C, 0.5 $mg\,cm^{-2}$) on the cathode. The porous transport layers (PTL) are carbon cloth (Sigracet 35DC) and titanium felt on the cathode and the anode, respectively. The Ti felt is 350 µm thick, with a porosity of 81% and a fiber diameter of 20 µm. Additionally, an Iridium contact layer is employed between the catalyst layer and the Ti-felt (2.48 $mg\,cm^{-2}$).

The test bench is designed so that the cell is heated by the feed water, which is held at a constant temperature. The temperature is monitored close to the water inlet channel at the anode and close to the hydrogen outlet channel at the cathode. The water flow is constant around 270 $mL\,min^{-1}$, which represents a high over-stoichiometry. That way, steady temperature is established and mass transport contributions are minimized.

A Gamry Reference 3000 potentiostat/galvanostat is used for all IV and EIS measurements in a two-electrode set-up, meaning that the anode is connected to the working electrode and the cathode acts as the reference electrode. Figure 1 illustrates the experimental set-up.

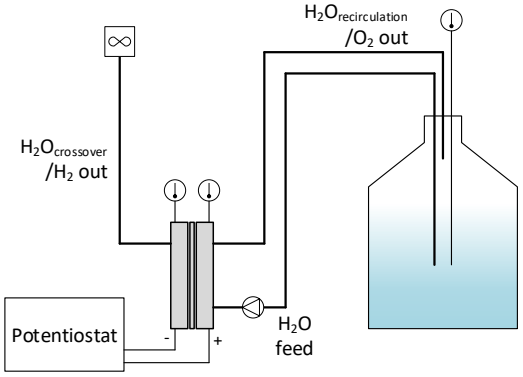

Figure 1: Test set-up including the cell, feed water tank, data acquisition, and power source.

Polarization curves are measured in variable steps of 0.01 $A\,cm^{-2}$ to 0.2 $A\,cm^{-2}$ in ascending direction. Each current step is held for 60 s before measuring the potential. The feed water flow rate is kept constant, which implies that the stoichiometry is in fact slightly changed throughout the experiment due to changes in current according to Faraday's law of electrolysis. However, the effect should not have a significant impact on the measurements since the over-stoichiometry is very high at any operation point with around 17000 at 1.0 $A\,cm^{-2}$.

Impedance spectra are, if not otherwise annotated, measured galvanostatic from 60 000 Hz to 0.1 Hz with 10 points per decade. The potentiostat supplies a variable AC disturbance current of 5% of the DC current operation point. The data is fit to an equivalent circuit as depicted in fig. 2. The circuit and its interpretation is discussed more in sections 3.2 and 3.3.

The MEA compression is controlled through the clamping pressure applied to the cell in eight steps (C0 to C7) according to tab. 1.

Estimating the actual clamping pressure applied to the MEA precisely is not as straight forward as it may seem. Additionally, the pressure distribution is generally a topic of interest which is investigated and opti-

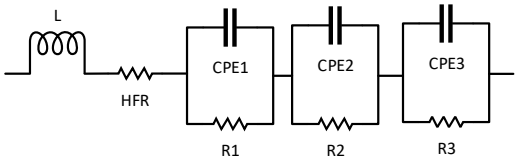

Figure 2: Equivalent circuit for impedance data fit

C0	C1	C2	C3
0.77 MPa	1.15 MPa	1.53 MPa	1.92 MPa

C4	C5	C6	C7
2.30 MPa	2.68 MPa	3.06 MPa	3.45 MPa

Table 1: Compression steps

mized experimentally, and through simulations [23, 24]. Different approaches in fuel cell research can be found in the literature, which can be transferred to electrolysis research. However, the mechanisms may not be strictly derived from fuel cells since the geometry and fluid compositions differ. Furthermore, it is arguable which area should be considered to calculate the compression. In this work, four die springs are used to establish a pressure distribution as homogeneous as possible. Actual compression pressure as well as homogeneity are tested ex-situ with a pressure sensitive film in sec. 3.1. The film exhibits a red color at points of pressure that is dependent on the pressure value. The color intensity was analyzed with image processing software and can be related to the applied pressure through reference curves supplied by the manufacturer.

Moreover, contact resistances are measured between several components that are accessible. Each contact is investigated separately through a sample with a high precision Ohmmeter while being clamped between two copper plates. The three experimentally determined contact resistances are between the anode bi-polar plate (BPP) and the anode current distributor (CD), between the anode BPP and the Ti felt, and between the cathode BPP and cathode CD.

2.1. Model Description

A 2-dimensional model approach is utilized in this study. The model is based on simulating the polarization curve of the cell at each operation point by fitting certain parameters. For a detailed description of the model development, the reader is referred to a previous publication [25]. The polarization curve is constructed through the Nernst potential raised by the losses. Due to the small geometry of the cell and the high overstoichiometry, only activation and ohmic losses are considered. The assumption of negligible mass transport losses is validated by the experimentally measured IV curves shown in figure 5. Since all experiments are carried out at atmospheric pressure, the cell potential can be calculated as:

$$E_{cell} = E_{Nernst}(T) + \eta_{act}(i, T) + \eta_{ohm}(i, T) \tag{1}$$

where i is the current density and T the temperature. The activation overpotential is estimated through the Butler-Volmer equation as [26]:

$$i = i_0 \cdot [e^{\alpha n F \eta/(RT)} - e^{-(1-\alpha) n F \eta/(RT)}] \tag{2}$$

where R and F have their common meaning, i_0 is the exchange current density, n the number of electrons, η the overpotential, and α is the charge transfer coefficient. The application of the Butler-Volmer equation assumes one rate determining step (rds) for the modelled reaction mechanism [27]. For the sake of modelling simplicity, α is therefore assumed to be constant over the whole current range [28, 29, 30].

The ohmic overpotential is simulated as:

$$\eta_{ohm} = i \cdot [R_m(T, \lambda) + R_c] \tag{3}$$

where R_m is the area specific membrane resistance and R_c the area specific contact resistance. The membrane resistance is implemented as a function of temperature and water content (λ). The model is utilized to fit the experimental data, where i_0, and R_c are the most important fitting parameters.

3. Results and Discussion

3.1. Compression Pressure Analysis

An ex-situ investigation on the compression pressure is carried out in order to validate the theoretical values as reported in tab. 1. Three layers of pressure sensitive film are placed within the cell: At the anode between flow field and Ti felt and between Ti felt and CL, and at the cathode between PTL and flow field.

Figure 3 indicates the applicability of the method. A higher compression force leads to a more intense red tone, and the contact-less channels between the land areas are visible as white areas, indicating no pressure. The experiment reveals the importance of the pressurization method. The cell in this study was clamped with four die springs.

Figure 3 (grey box) shows the pressure distribution at compression step four (C4) for all three locations. As it can be seen, the cathode side (bottom) exhibits the channels clearly, suggesting that only the land area compresses the MEA. Similar results can be seen at the anode between the BPP and the PTL (middle), where the significantly smaller channels are still clearly visible. The situation changes when comparing to the result between the PTL and the CL at the anode side (top), where the distribution is more uniform and only the cathode-side flow channels can be identified. This can be seen as a confirmation that the Ti felt serves the purpose of uniformly distributing the contact points (and therefore current and fluids) from the BPP to the electrode. The figure also shows the anode-side film after each compression step was applied (left to right), where the last compression step was not experimentally determined due to restrictions in the pressure range of the film.

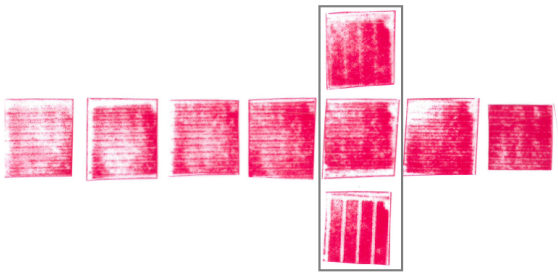

Figure 3: Pressure sensitive film after being clamped between the anode BPP and PTL at C0 to C6 (middle series). For comparison: Between anode PTL and CL (top), and cathode PTL and BPP (bottom) at C4

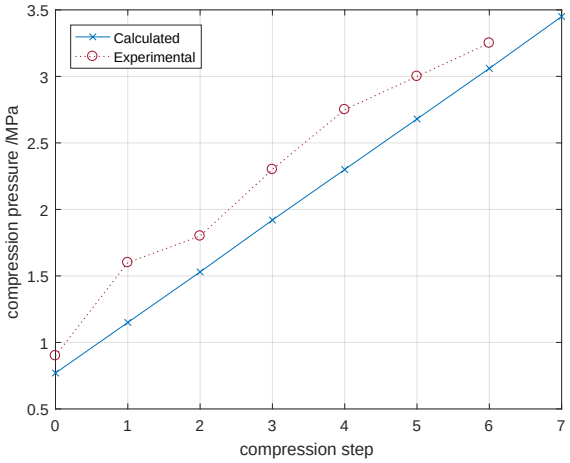

Figure 4: Comparison of calculated and experimentally determined compression pressure

The applied pressure is not always uniformly distributed, but can be considered sufficient for this work. A non-homogeneous compression may lead to local hot spots and can affect the lifetime of the cell considerably [31]. Figure 4 summarizes the comparison between the experimentally extracted compression pressure for each step compared to the calculated ones. It has to be noted that the experimental determination underlies some uncertainties and can only be seen as an indication. The film itself is rated with ±10% accuracy, but is highly affected by environmental influences such as temperature and humidity. Furthermore, the value for the pressure is extracted as an average over the land area of the flow field, i.e., assuming homogeneous compression and neglecting the area of the channels. As indicated above, the stiff Ti felt distributes the pressure sufficiently well to make this assumption acceptable. It can be seen in the figure that the experimental determination overestimates the values, or that the calculated values are slightly too low, respectively. However, the linear trend is visible and changes in compression are reasonably captured. For further analysis the calculated values are chosen as tabulated in tab. 1.

3.2. Polarization Curves and Electrochemical Impedance Spectroscopy

The performance of the single cell in terms of polarization curves is shown in fig. 5. The figure includes the plots for all eight compressions at both temperatures 60 °C and 80 °C.

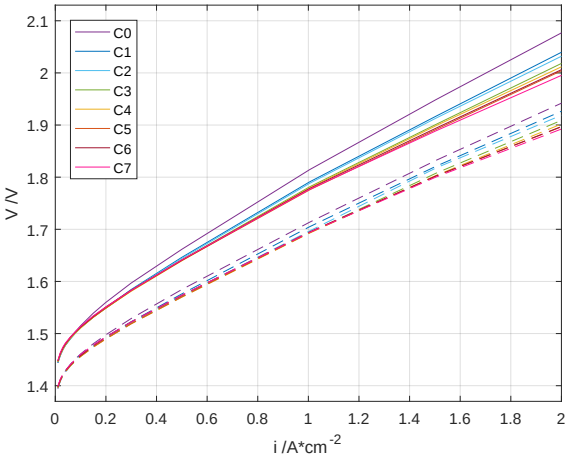

Figure 5: Polarization curves for all compressions at 60 °C (solid) and 80 °C (dashed)

Generally, the cell exhibits close to state of the art performance at both temperatures, with a voltage at 2.0 A cm^{-2} of 2.01 V at 60 °C and 1.90 V at 80 °C at

medium compression (C4) [32, 33]. The positive effect of increased temperature can be seen easily. This behavior is expected due to better reaction kinetics for both hydrogen evolution reaction (HER) and oxygen evolution reaction (OER) [2], and better membrane conductivity [34]. This is also confirmed by the impedance data, which was systematically recorded at several operation points. For the impedance analysis, only the values for high frequency resistance (HFR) and low frequency resistance (LFR) are considered. Figure 6 exemplary shows the impedance data together with their model fits as a Nyquist plot for different currents at C4 and both temperatures.

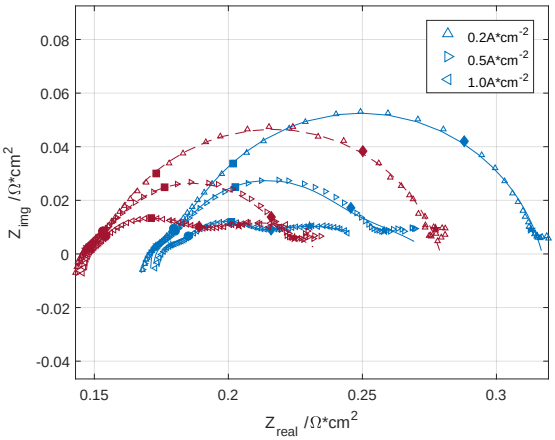

Figure 6: Impedance data at C4 and different currents as a Nyquist plots. The marks represent the frequencies 10 000 Hz (∗), 1000 Hz (•), 100 Hz (■), 10 Hz (⧫), and 1 Hz (⋆). The respective model fits are shown for both 60 °C (solid) and 80 °C (dashed).

HFR and LFR represent the intercepts of the Nyquist plot with the x-axis at high frequency (left) and low frequency (right), respectively. The HFR represents the total area normalized ohmic resistance within cell, which includes the membrane resistance (both to electron and proton transport), material resistance of the components, and contact resistances. Other sources are assumed to be negligible. The LFR moreover includes the polarization resistance of the cell.

It can be seen that the HFR decreases with increasing temperature at the same current operation point. That supports the claim of better membrane conductivity at elevated temperatures. The LFR shifts accordingly, but when comparing the difference between HFR and LFR at the two temperatures, a decrease of around 6 mΩ cm^2 can be observed. This difference is an indication of better reaction kinetics at elevated temperatures.

It can furthermore be seen that the Nyquit plots exhibit different characteristics depending on the operation condition. On first sight, it seems that between the high- and low frequency intercepts, two to three semi-circles can be distinguished. Low current operation (0.2 A cm^{-2}) shows a small semi-circle in the high-frequency area (>10 kHz), followed by one big semi-circle in the mid-frequency area and relatively indistinguishable shape in the at low frequencies (<1 Hz). With increasing current, while the high frequency arc remains unaltered, the second semi circle shrinks, and a third semi-circle appears and becomes more evident at around 1 A cm^{-2}. The shrinking of an arc in the Nyquist plot signifies decreased impedance, and therefore, increase in reaction processes. Even though, the low frequency arc is usually associated with mass transport losses in the fuel cell literature [12], in the current work where high over stoichiometry is used, the evolution of the third arc may be explained differently.

As the LFR represents the total polarization resistance including the HFR parts, the value should be equal to the slope of the polarization curve according to

$$R_{pol} = \frac{\Delta U}{\Delta i} = LFR \tag{4}$$

Therefore, the two values should be in agreement. Figure 7 shows, that the LFR is slightly smaller than the IV slope throughout the whole current range at both temperatures. The slow EIS measurements at low frequencies (<1 Hz) are far more affected by noise compared to the fast measurements at high frequencies. That as well as the fitting procedure for the LFR can induce errors in the measurement. However, since the difference seems to be systematic (all values are smaller), the cause may not solely lie within inaccuracies. Although the phenomenon was also observed by some fuel cell researchers [35], no commonly agreed explanation can be found in the literature, while other authors found the two resistances to be equal both in FC and WE research [36, 37]. A full paper dedicated to the topic for FC can be found in [35]. The authors connect the difference to the reactant feed mode and account for it through a model. In this work, the difference is within a 12% margin.

When focusing on the less researched effect of cell compression, the first impression from the polarization curves is that a higher compression has a positive effect on the cell performance at higher currents. The differences in voltage at 2.0 A cm^{-2} at lowest compression compared to highest compression at 60 °C and 80 °C are 81 mV and 49 mV, respectively. This effect seems to vanish or even reverse at lower current operation points. Therefore, it can be concluded that the improved per-

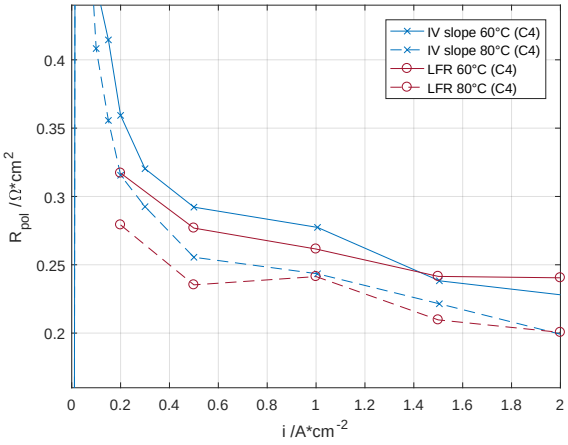

Figure 7: Polarization resistance from IV slopes (X) and LFR (O) at 60 °C (solid) and 80 °C (dashed) at C4 for both temperatures

formance is mainly due to decrease in the total ohmic resistance within the cell.

3.3. Model Supported Analysis

To allow for a more detailed analysis on the effect of compression on the cell performance, two modelling approaches are followed based on the two characterization methods: First, the electrical equivalent circuit (EEC) as shown in figure 2 is fit with EIS data. Second, the model proposed in section 2.1 is fit with polarization data. Since no reference electrode is incorporated into the cell, all measurements refer to the whole cell assembly including anode and cathode contributions.

Fitting impedance data to an EEC is a highly sensitive process with multiple sources of errors. The fundamental problem is that most circuit components cannot be connected to an actual cell component. While HFR was introduced earlier and can be justified through the existence of purely ohmic components, the other elements have to be further explained. Many authors, especially in FC research, use two RC-loops and refer to them as anode- and cathode- contributions [38]. This assumption may be supported by the development of a mechanistic model, which results in a similar EEC [39], but cannot overcome the problem of multiple fitting solutions. Sometimes, the hydrogen oxidation reaction at the anode is considered orders of magnitude faster compared to the oxygen reduction reaction at the cathode and therefore neglected [40]. The capacitance then embodies the double layer capacitance at the electrode interface, where the resistance represents the charge transfer resistance. Often, the capacitor is replaced by a constant-phase element (CPE), which represents a non-uniformly distributed double layer that appears as a depressed semi-circle in a Nyquist plot [41, 42]. Generally, R//C-circuits (or R//CPE-circuits) can be associated to characteristic frequency regions, and therefore, represent processes of different time constants. These can include different reaction mechanisms, different steps of a certain reaction, or diffusion processes. Finally, the inductor in series with the HFR represents possible inductive parts of cables and other components that can be observed in the impedance data.

The observation from the IV curves that an increased compression leads to reduced ohmic resistance, is validated by the impedance data. Figure 8 shows the HFR as a function of applied pressure for both temperatures at 1.0 A cm^{-2}.

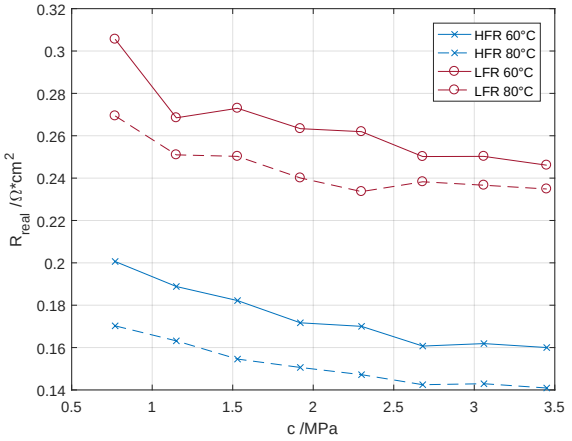

Figure 8: HFR (X) and LFR (O) at 60 °C (solid) and 80 °C (dashed) at 1.0 A cm^{-2}

The HFR decreases both with increasing temperature and increasing compression. Since the HFR represents only ohmic resistances, the decrease with temperature can be connected to the increased conductivity of the membrane [43]. For C0, the HFR drops from 201 mΩ cm^2 at 60 °C to 170 mΩ cm^2 at 80 °C. At higher temperatures, not only do the absolute resistance values decrease with increasing compression, but also the achieved enhancements decrease. For example, the enhancement from 60 °C to 80 °C for C0 is around 30 mΩ cm^2, but it drops to around 20 mΩ cm^2 for C7, which has resistance value of 160 mΩ cm^2 at 60 °C and 141 mΩ cm^2 at 80 °C. That means, the compression-related benefits are more pronounced at lower temperatures.

However, the HFR at both temperatures clearly decreases with increased compression. Following a non-linear relationship, the HFR at C7 and 60 °C drops to around 80% of its value at C0. At 80 °C, the HFR drops to around 83%. The results are in line with the find-

ings from the IV curves and support the idea that higher compressions lead to lower ohmic losses. Two major reasons may be assumed to contribute to that: A higher membrane compression shortens the distance for protons to travel, i.e. leads to a lower overpotential. Additionally, an increased clamping pressure lowers the contact resistances between the components. The first cause is rejected, as the membrane compression has a negative effect on the water uptake, which overwhelms the positive effect of lower thickness (see figure 10). On the other hand, as it is known from fuel cell research, the electrical contacts between the several solid layers are highly influenced by the compression [20].

Many studies suggest that the compression is subject to optimization, as the contact resistance decreases logarithmic to a certain minimum, while other parameters may affect the cell performance negatively. As an example, the gas diffusion layers (GDL) may be crushed and pushed into the channels, which results in mass transport problems. Although the materials are not exactly the same and partly serve a different purpose compared to fuel cells, the general principles may be transferred. The gas diffusion layers are somewhat equivalent to the PTL in WE, where the cathode side PTL in this case is made of the same material as common GDL for fuel cells. In order to further investigate the influence of compression, temperature, and current, the proposed model is utilized to extract several parameters from the polarization data.

The extracted parameters of major interest are the exchange current density (i_0) and the contact resistance (R_c), which are shown in figure 9 for all compressions. Note that the reported i_0 is the reference value at 25 °C and implemented as a function of temperature, where R_c is temperature independent. Furthermore, the fit value for the activation energy E_{act} is 0.103 455 MJ mol^{-1} and the symmetry factor β is 0.4931

It can be seen that the overall contact resistance steadily decreases with increasing compression. With a value of 65.3 mΩ cm^2 at C0 and 52.9 mΩ cm^2 at C7, the reduction accounts for around 19% of its original value.

In the meanwhile, the exchange current density experiences an increase up to around 1.5 MPa (C2), followed by a steady decrease up to the highest compression. In this figure, i_0 represents the apparent exchange current density. That means, the related area does not represent the active area of the cell, but can rather be seen as the electrochemical surface area (ECSA), which includes the surface roughness of the layers. An increase in ECSA implies an increase in the apparent exchange current and therefore an increase in performance. From

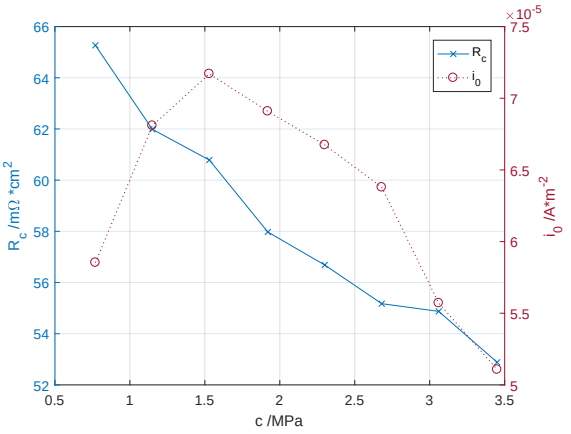

Figure 9: Model fits for contact resistance (solid) and the apparent reference exchange current density at 25°C (dotted)

the lowest compression up to 1.5 MPa, an increase in ECSA may be deduced from the figure. As the Ti felt on one hand and the carbon cloth on the other get pressed against the respective catalyst layers, the electrochemically active area may increase. Voids between these layers may be filled and the three phase boundary is increased. At a certain point, the compression may get high enough to not only increase the surface area, but also start crushing the porous PTLs, especially the carbon at the cathode side. In turn, the ECSA decreases as the surfaces smooths, and the exchange current decreases as seen in the figure. Although not observed in this work, a high compression may also lead to increased mass transport problems, as the porosity of the PTLs decrease. Furthermore, it may facilitate degradation, as hot sports are more likely to occur due to mechanical wear down [44].

3.4. Contact Resistances

It is furthermore attempted to separate the total ohmic resistance (HFR) into its main contributors as follows:

$$R_{ohm} = R_{m,H^+} + R_c + R_{components} \tag{5}$$

Figure 10 shows the total ohmic resistance of the cell together with the respective contributions of the membrane and the contacts as predicted by the model. For comparison, the HFR extracted from the impedance data is also plotted.

The membrane compression has a negative effect on the water uptake (λ) of the Nafion, where a lower λ decreases the conductivity, despite the positive effect of a slightly lower thickness. Therefore, the membrane resistance increases slightly over the compression range.

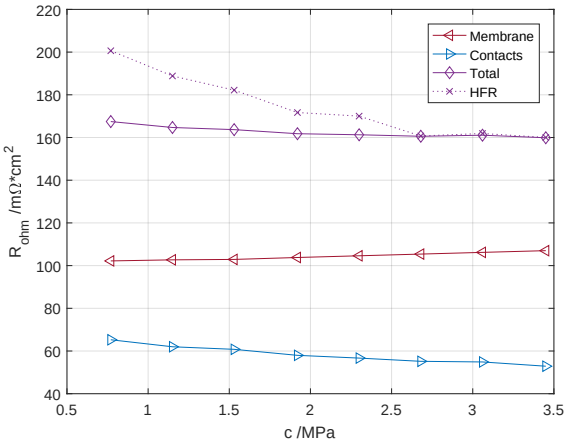

Figure 10: Breakdown of ohmic resistance between the two major contributors membrane and contacts at 60 °C

However, a positive effect on the cell performance can be observed due to decreasing contact resistance with increasing compression. Figure 10 reveals, that the decrease of ohmic resistance can be solely attributed to contact resistances. To further investigate the contacts, ex-situ measurements are carried out.

Figure 11 shows the three contact resistances as experimentally determined. All measurements were taken at room temperature (25 °C). For comparison, the model prediction for the total contact resistance is also included.

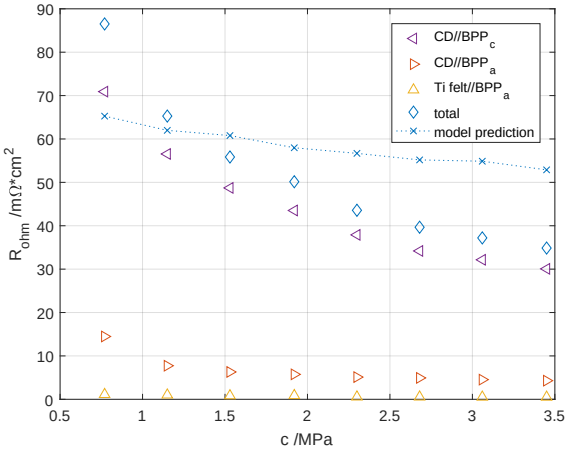

Figure 11: Contact resistances measured ex-situ. The model predictions are added for comparison

The measurements reveal that the contact between the carbon BPP on the cathode side and the the respective CD accounts for the highest share. Somewhat surprisingly, the cell under investigation here does not show a significant contribution of the anodic PTL (Ti felt) as found by other studies [45]. The reason may be the incorporated Ir metal layer between the CL and the PTL on the anode, which is a relatively unique feature. The total values predicted by the model are higher than the experimental values for most compressions. It has to be kept in mind, that the model summarizes all contact resistances as one, where only three contacts are determined experimentally due to accessibility of the layers. The contacts between the catalyst layers on anode and cathode side add to the total value, as well as the cathode-side PTL contacts. Furthermore, the model as it is constructed assumes a constant charge transfer coefficient and may therefore overestimate the contact resistance as a result of applying the Butler-Volmer equation to the multi-electron transfer reactions. Therefore, the here suggested contact resistance and the further indicated share of roughly 2/3 to 1/3 for the membrane and the contacts, respectively, may be analyzed with care. The next section explains the problems by analyzing possible reaction mechanisms further.

3.5. Tafel Plot Analysis

The overall process of splitting water in a PEM electrolysis cell can be described as

$$2\,H_2O \longrightarrow 2\,H_2 + O_2$$

The two half-cell reactions at the anode and cathode are the oxygen evolution reaction (OER) and hydrogen evolution reaction (HER), respectively. The HER is fast due to the relatively high exchange current density and the high reversibility. The OER is somewhat more sluggish and less well understood [2]. However, different reaction mechanisms were proposed and table 2 summarizes one that is believed to occur in the given environment. That means acidic media, and an Iridium-based catalyst for the OER. For the following discussion, the cathode is considered as a reference electrode. Therefore, all observations are attributed to the OER, where the HER is neglected here, since it is assumed to only play a minor role for the characterization [46, 14].

Step	Reaction
(1)	$S + H_2O \longrightarrow S-OH + H^+ + e^-$
(2)	$S-OH \longrightarrow S-O^- + H^+ + e^-$
(3)	$2\,S-O \longrightarrow S + O_2$

Table 2: Reaction mechanism for OER under PEM WE environment

Depending on which step is the rate determining step (*rds*), a theoretical Tafel slope for the reaction can be calculated and compared to the experimentally determined slope, which may give insight into the re-

action mechanism. Tafel slopes of 132 mV/dec and 44 mV/dec should be observed at 60 °C for the first and the second step as *rds*, respectively. However, the experimental determination of the Tafel slope is not trivial, and controversially discussed in the literature. The discord already starts with how to correctly account for the ohmic (*iR*) correction of the potential. Where many examples of using the purely ohmic resistance of the HFR (or equivalently the current step response) can be found [47, 28, 48, 49], it is also conceivable to compensate for the total cell resistance represented by the LFR (or IV slope), since it may contain ohmic contributions from components of the cell other than the membrane and contacts. An example could be the ionic conduction within the Nafion catalyst binder [50, 37].

The Tafel plots including linear trendlines for both approaches (HFR and LFR correction) at C4 together with a Butler-Volmer approximation are shown in figure 12a. It can be seen, that the HFR-corrected plot exhibits two slopes, where the LFR-corrected plot seems to have only one. The two points at high currents could be explained by the fact that the actual LFR is decreasing with current, where here an average is chosen. The slope of the LFR-corrected plot is very similar to the first slope of the HFR-corrected plot with 43 mV/dec and 45 mV/dec, respectively. The value is also coherent with what is expected from the theoretical calculation when assuming step (2) to be rate determining. From the Tafel slopes, the charge transfer coefficient α can be estimated (not to be confused with the symmetry factor β). The parameter reveals insights into the reaction mechanism, symmetry, and number of exchanged electrons [51, 52, 53]. The single slope for the LFR-corrected plot implies a constant charge transfer coefficient and therefore supports the presented model approach. However, HFR-correction as well as the presence of more than one Tafel slope can be found throughout the literature [54, 55]. One explanation is to connect the deviation from what the Tafel equation predicts at higher currents to mass transport phenomena [28]. However, in this work mass transport problems are excluded due to high over-stoichiometry, interdigitated feed water channels, a small cell geometry, and a high anode PTL porosity [56]. Additionally, no evidence for mass transport problems were found in the recorded IV curves or impedance spectra. That being said, the second slope with 158 mV/dec may indicate a change in the OER *rds* from one at lower potentials to another one at higher potentials.

On the other hand, when looking at figure 12b, where the HFR-corrected Tafel plots at C4 and C7 are shown, it seems that while the first slope is compression-

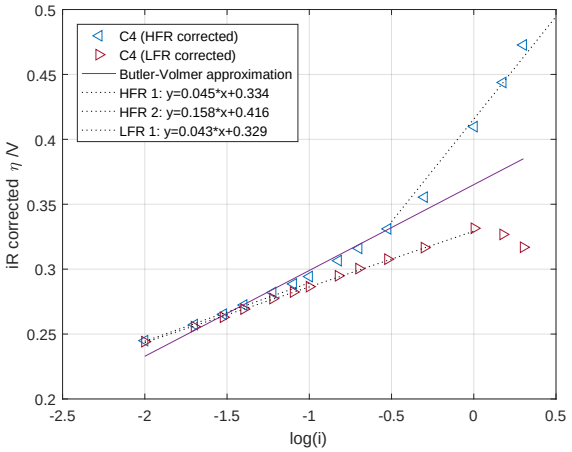

(a) Comparison between HFR- and LFR-correction at C4

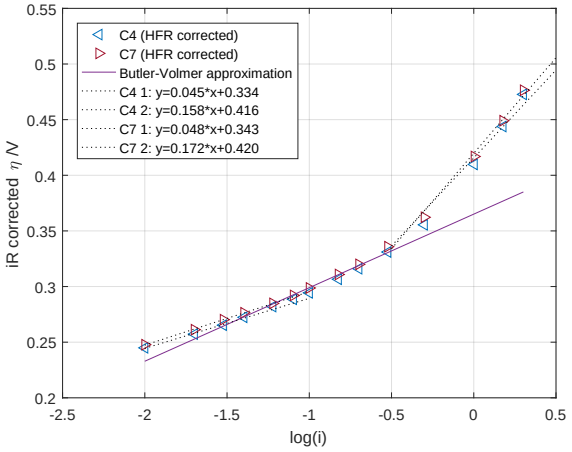

(b) Comparison between C4 and C7 (HFR-correction)

Figure 12: Tafel plots at 60°C with their respective linear approximations. The Butler-Volmer relation is added for comparison.

independent (variation of 3 mV/dec), the second slope is in fact slightly affected by the cell compression (variation of 14 mV/dec). That would suggest a more ohmic nature of the overpotential at higher current. A similar suggestion can be found in FC research, where a distinction is made between the non-electrode ohmic resistance, and the electrode ohmic resistance [57]. Where the non-electrode related share was found through the current interrupt method, the electrode related share was developed through oxygen reduction reaction and Ficks law of diffusion. A similar process may be present in PEM WE, although mass transport phenomena are neglected in the present work. It remains for future work to develop a model similar to what is shown for FC to precisely correct for the ohmic voltage drop [58]. Since the compression can also affect electrochemical param-

eters such as the exchange current density (see fig. 9), a change in reaction mechanism may also not be ruled out completely.

Additionally to the experimental Tafel plots, figure 12 shows the Butler-Volmer equation with the constant parameters apparent charge transfer coefficient and exchange current density as predicted by the model before. By comparison to the experimental data, it becomes clear why the model underpredicts the activation overpotential if a change in rds is assumed. Therefore, electrochemical processes are attributed the the ohmic contact resistance as R_c is the fit value. Further investigations on the the nature of the reaction mechanisms are necessary to prove or rule out one of the presented options.

4. Conclusion

The effect of clamping pressure at various currents and temperatures on a state of the art PEM WE cell were investigated. Where a clear influence can already be seen in the polarization curves, electrochemical impedance spectroscopy and Tafel plots were utilized to further narrow down the analysis. Additionally, a mathematical model was utilized to extract exchange current density and contact resistance. The exchange current density seems to have an optimal value of compression at around 1.5 MPa, where the contact resistance decreases throughout the whole range of investigated compressions. That was further supported by ex-situ contact resistance measurements. Compared to the contacts, the membrane is the dominant contributor to the ohmic losses within the cell. A Tafel plot analysis revealed a certain disagreement in the literature. The proposed explanations include a change in rate determining step for the oxygen evolution reaction.

Besides the positive effect on cell performance, it should be kept in mind, that both increased temperature and compression may have a negative effect on the lifetime of the cell due to formation of hot spots. That is investigated in on-going work.

Acknowledgement

The authors would like to acknowledge the support by Innovation Fund Denmark through the e-STORE project, Grant 4106-00025B.

References

[1] International Energy Agency (IEA), Technology Roadmap: Hydrogen and Fuel Cells, Tech. rep., IEA (2015). doi:10.1007/SpringerReference_7300.

[2] A. Godula-Jopek, Hydrogen Production by Electrolysis, Wiley-VCH, 2015.

[3] F. Gutiérrez-Martín, I. Guerrero-Hernández, Balancing the grid loads by large scale integration of hydrogen technologies: The case of the Spanish power system, International Journal of Hydrogen Energy 37 (2) (2012) 1151–1161. doi:10.1016/j.ijhydene.2011.09.116.

[4] D. Bessarabov, H. Wang, H. Li, N. Zhao, PEM Electrolysis for Hydrogen Production - Principles and Applications, CRC Press, 2016.

[5] M. Carmo, D. L. Fritz, J. Mergel, D. Stolten, A comprehensive review on PEM water electrolysis, International Journal of Hydrogen Energy 38 (12) (2013) 4901–4934.

[6] F. Barbir, PEM electrolysis for production of hydrogen from renewable energy sources, Solar Energy 78 (5) (2005) 661–669. doi:10.1016/j.solener.2004.09.003.

[7] S. A. Grigoriev, V. I. Porembskiy, S. V. Korobtsev, V. N. Fateev, F. Aupre, P. Millet, High-pressure PEM water electrolysis and corresponding safety issues, International Journal of Hydrogen Energy 6 (2010) 3–10. doi:10.1016/j.ijhydene.2010.03.058.

[8] B. Bensmann, R. Hanke-Rauschenbach, I. K. Peña Arias, K. Sundmacher, Energetic evaluation of high pressure PEM electrolyzer systems for intermediate storage of renewable energies, Electrochimica Acta 110 (2013) 570–580. doi:10.1016/j.electacta.2013.05.102.

[9] F. N. Büchi, S. A. Freunberger, M. Reum, G. Paganelli, A. Tsukada, P. Dietrich, A. Delfino, On the efficiency of an advanced automotive fuel cell system, Fuel Cells 7 (2) (2007) 159–164. doi:10.1002/fuce.200500257.

[10] A. S. Arico, S. Siracusano, N. Briguglio, V. Baglio, A. Di Blasi, V. Antonucci, Polymer electrolyte membrane water electrolysis: Status of technologies and potential applications in combination with renewable power sources, Journal of Applied Electrochemistry 43 (2) (2013) 107–118. doi:10.1007/s10800-012-0490-5.

[11] C. A. Martinson, G. van Schoor, K. R. Uren, D. Bessarabov, Characterisation of a PEM electrolyser using the current interrupt method, International Journal of Hydrogen Energy 39 (36) (2014) 20865–20878. doi:10.1016/j.ijhydene.2014.09.153.
URL http://dx.doi.org/10.1016/j.ijhydene.2014.09.153

[12] X. Yuan, H. Wang, J. Colinsun, J. Zhang, AC impedance technique in PEM fuel cell diagnosisA review, International Journal of Hydrogen Energy 32 (17) (2007) 4365–4380. doi:10.1016/j.ijhydene.2007.05.036.

[13] J. Wu, X. Z. Yuan, H. Wang, M. Blanco, J. J. Martin, J. Zhang, Diagnostic tools in PEM fuel cell research: Part I Electrochemical techniques, International Journal of Hydrogen Energy 33 (6) (2008) 1735–1746. doi:10.1016/j.ijhydene.2008.01.013.

[14] C. Rozain, P. Millet, Electrochemical characterization of Polymer Electrolyte Membrane Water Electrolysis Cells, Electrochimica Acta 131 (2014) 160–167. doi:10.1016/j.electacta.2014.01.099.
URL http://dx.doi.org/10.1016/j.electacta.2014.01.099

[15] J. Van Der Merwe, K. Uren, G. Van Schoor, D. Bessarabov, Characterisation tools development for PEM electrolysers, International Journal of Hydrogen Energy 39 (26) (2014) 14212–14221. doi:10.1016/j.ijhydene.2014.02.096.
URL http://dx.doi.org/10.1016/j.ijhydene.2014.02.096

[16] H. Su, B. J. Bladergroen, S. Pasupathi, V. Linkov, S. Ji, Performance investigation of membrane electrode assemblies for hydrogen production by solid polymer electrolyte water electrolysis, International Journal of Electrochemical Science 7 (5) (2012) 4223–4234.

[17] B. S. Lee, H. Y. Park, I. Choi, M. K. Cho, H. J. Kim, S. J. Yoo, D. Henkensmeier, J. Y. Kim, S. W. Nam, S. Park, K. Y. Lee, J. H. Jang, Polarization characteristics of a low

catalyst loading PEM water electrolyzer operating at elevated temperature, Journal of Power Sources 309 (2016) 127–134. doi:10.1016/j.jpowsour.2015.12.139.
URL http://dx.doi.org/10.1016/j.jpowsour.2015.12.139

[18] I. Dedigama, P. Angeli, K. Ayers, J. B. Robinson, P. R. Shearing, D. Tsaoulidis, D. J. L. Brett, In situ diagnostic techniques for characterisation of polymer electrolyte membrane water electrolysers - Flow visualisation and electrochemical impedance spectroscopy, International Journal of Hydrogen Energy 39 (9) (2014) 4468–4482. doi:10.1016/j.ijhydene.2014.01.026.
URL http://dx.doi.org/10.1016/j.ijhydene.2014.01.026

[19] S. Sun, Y. Xiao, D. Liang, Z. Shao, H. Yu, M. Hou, B. Yi, Behaviors of a proton exchange membrane electrolyzer under water starvation, RSC Adv. 5 (19) (2015) 14506–14513. doi:10.1039/C4RA14104K.
URL http://xlink.rsc.org/?DOI=C4RA14104K

[20] J. Millichamp, T. J. Mason, T. P. Neville, N. Rajalakshmi, R. Jervis, P. R. Shearing, D. J. L. Brett, Mechanisms and effects of mechanical compression and dimensional change in polymer electrolyte fuel cells - A review, Journal of Power Sources 284 (2015) 305–320. doi:10.1016/j.jpowsour.2015.02.111.
URL http://dx.doi.org/10.1016/j.jpowsour.2015.02.111

[21] S. Asghari, A. Mokmeli, M. Samavati, Study of PEM fuel cell performance by electrochemical impedance spectroscopy, International Journal of Hydrogen Energy 35 (17) (2010) 9283–9290. doi:10.1016/j.ijhydene.2010.03.069.
URL http://dx.doi.org/10.1016/j.ijhydene.2010.03.069

[22] A. Diedrichs, M. Rastedt, F. J. Pinar, P. Wagner, Effect of compression on the performance of a HT-PEM fuel cell, Journal of Applied Electrochemistry 43 (11) (2013) 1079–1099. doi:10.1007/s10800-013-0597-3.

[23] A. Bates, S. Mukherjee, S. Hwang, S. C. Lee, O. Kwon, G. H. Choi, S. Park, Simulation and experimental analysis of the clamping pressure distribution in a PEM fuel cell stack, International Journal of Hydrogen Energy 38 (15) (2013) 6481–6493. doi:10.1016/j.ijhydene.2013.03.049.
URL http://dx.doi.org/10.1016/j.ijhydene.2013.03.049

[24] E. Alizadeh, M. Ghadimi, M. M. Barzegari, M. Momenifar, S. H. Saadat, Development of contact pressure distribution of PEM fuel cell's MEA using novel clamping mechanism, Energy 131 (2017) 92–97. doi:10.1016/j.energy.2017.05.036.
URL http://dx.doi.org/10.1016/j.energy.2017.05.036

[25] A. C. Olesen, S. K. Kær, The Effect of PFSA Membrane Compression on the Predicted Performance of a High Pressure PEM Electrolysis Cell, ECS Transactions 68 (3) (2015) 99–116. doi:10.1149/06803.0099ecst.

[26] R. O'Hayre, S.-W. Cha, W. Colella, F. B. Prinz, Fuel Cell Fundamentals, John Wiley and Sons, 2006.

[27] R. F. Mann, J. C. Amphlett, B. A. Peppley, C. P. Thurgood, Application of Butler Volmer equations in the modelling of activation polarization for PEM fuel cells, Journal of Power Sources 161 (2006) 775–781. doi:10.1016/j.jpowsour.2006.05.026.

[28] M. Suermann, T. J. Schmidt, F. N. Büchi, Cell Performance Determining Parameters in High Pressure Water Electrolysis, Electrochimica Acta 211 (2016) 989–997. doi:10.1016/j.electacta.2016.06.120.

[29] F. Marangio, M. Santarelli, M. Calì, Theoretical model and experimental analysis of a high pressure PEM water electrolyser for hydrogen production, International Journal of Hydrogen Energy 34 (3) (2009) 1143–1158. doi:10.1016/j.ijhydene.2008.11.083.

[30] Z. Abdin, C. J. Webb, E. M. Gray, Modelling and simulation of a proton exchange membrane (PEM) electrolyser cell, International Journal of Hydrogen Energy 40 (39) (2015) 13243–13257. doi:10.1016/j.ijhydene.2015.07.129.
URL http://dx.doi.org/10.1016/j.ijhydene.2015.07.129

[31] T. Hottinen, O. Himanen, S. Karvonen, I. Nitta, T. Hottinen, O. Himanen, M. Mikkola, S. Karvonen, I. Nitta, Inhomogeneous compression of PEMFC gas diffusion layer. Part II. Modeling the effect, Journal of Power Sources 171 (1) (2007) 113–121.

[32] C. Rozain, E. Mayousse, N. Guillet, P. Millet, Influence of iridium oxide loadings on the performance of PEM water electrolysis cells : Part I Pure IrO 2 -based anodes, "Applied Catalysis B, Environmental" 182 (2016) 153–160. doi:10.1016/j.apcatb.2015.09.013.
URL http://dx.doi.org/10.1016/j.apcatb.2015.09.013

[33] S. Siracusano, V. Baglio, E. Moukheiber, L. Merlo, A. S. Arico, Performance of a PEM water electrolyser combining an IrRu-oxide anode electrocatalyst and a shortside chain Aquivion membrane, International Journal of Hydrogen Energy 40 (42) (2015) 14430–14435. doi:10.1016/j.ijhydene.2015.04.159.

[34] T. a. Zawodzinski, Water Uptake by and Transport Through Nafion® 117 Membranes, Journal of The Electrochemical Society 140 (4) (1993) 1041. doi:10.1149/1.2056194.

[35] M. Chandesris, C. Robin, M. Gerard, Y. Bultel, Investigation of the difference between the low frequency limit of the impedance spectrum and the slope of the polarization curve, Electrochimica Acta 180 (2015) 581–590. doi:10.1016/j.electacta.2015.08.089.
URL http://dx.doi.org/10.1016/j.electacta.2015.08.089

[36] I. Pivac, F. Barbir, Inductive phenomena at low frequencies in impedance spectra of proton exchange membrane fuel cells - A review, Journal of Power Sources 326 (2016) 112–119. doi:10.1016/j.jpowsour.2016.06.119.
URL http://dx.doi.org/10.1016/j.jpowsour.2016.06.119

[37] K. Elsøe, L. Grahl-Madsen, G. G. Scherer, J. Hjelm, M. B. Mogensen, Electrochemical Characterization of a PEMEC Using Impedance Spectroscopy, Journal of The Electrochemical Society 164 (13) (2017) F1419–F1426. doi:10.1149/2.0651713jes.
URL http://jes.ecsdl.org/lookup/doi/10.1149/2.0651713jes

[38] A. M. Dhirde, N. V. Dale, H. Salehfar, M. D. Mann, T. H. Han, Equivalent electric circuit modeling and performance analysis of a PEM fuel cell stack using impedance spectroscopy, IEEE Transactions on Energy Conversion 25 (3) (2010) 778–786. doi:10.1109/TEC.2010.2049267.

[39] S. M. R. Niya, R. K. Phillips, M. Hoorfar, Process modeling of the impedance characteristics of proton exchange membrane fuel cells, Electrochimica Acta 191 (2016) 594–605. doi:10.1016/j.electacta.2016.01.128.

[40] M. A. Rubio, A. Urquia, R. Kuhn, S. Dormido, Electrochemical parameter estimation in operating proton exchange membrane fuel cells, Journal of Power Sources 183 (1) (2008) 118–125. doi:10.1016/j.jpowsour.2008.05.011.

[41] M. E. Orazem, N. Pebere, B. Tribollet, Enhanced Graphical Representation of Electrochemical Impedance Data, Journal of The Electrochemical Society 153 (4) (2006) 129. doi:10.1149/1.2168377.

[42] P. Córdoba-Torres, T. J. Mesquita, O. Devos, B. Tribollet, V. Roche, R. P. Nogueira, On the intrinsic coupling between constant-phase element parameters ?? and Q in electrochemical impedance spectroscopy, Electrochimica Acta 72 (2012) 172–178. doi:10.1016/j.electacta.2012.04.020.
URL http://dx.doi.org/10.1016/j.electacta.2012.04.020

[43] H. Ito, T. Maeda, A. Nakano, H. Takenaka, Properties of Nafion membranes under PEM water electrolysis conditions, International Journal of Hydrogen Energy 36 (17) (2011) 10527–10540. doi:10.1016/j.ijhydene.2011.05.127.
URL http://dx.doi.org/10.1016/j.ijhydene.2011.05.127

[44] Q. Feng, X. Yuan, G. Liu, B. Wei, Z. Zhang, H. Li, H. Wang, A review of proton exchange membrane water electrolysis on degradation mechanisms and mitigation

strategies, Journal of Power Sources 366 (2017) 33–55. doi:10.1016/j.jpowsour.2017.09.006.
URL http://dx.doi.org/10.1016/j.jpowsour.2017.09.006

[45] P. Lettenmeier, S. Kolb, F. Burggraf, A. S. Gago, K. A. Friedrich, Towards developing a backing layer for proton exchange membrane electrolyzers, Journal of Power Sources 311 (2016) 153–158. doi:10.1016/j.jpowsour.2016.01.100.
URL http://dx.doi.org/10.1016/j.jpowsour.2016.01.100

[46] E. Brightman, J. Dodwell, N. Van Dijk, G. Hinds, In situ characterisation of PEM water electrolysers using a novel reference electrode, Electrochemistry Communications 52 (2015) 1–4. doi:10.1016/j.elecom.2015.01.005.
URL http://dx.doi.org/10.1016/j.elecom.2015.01.005

[47] K. S. Kadakia, P. Jampani, O. I. Velikokhatnyi, M. K. Datta, S. J. Chung, J. a. Poston, A. Manivannan, P. N. Kumta, Nanostructured (Ir,Sn)O2:F - Oxygen Evolution Reaction Anode Electro-Catalyst Powders for PEM Based Water Electrolysis, Journal of the Electrochemical Society 161 (9) (2014) F868–F875. doi:10.1149/2.0381409jes.
URL http://jes.ecsdl.org/cgi/doi/10.1149/2.0381409jes

[48] Gamry Instruments, Understanding iR Compensation (2017).

[49] A. J. Bard, G. Inzelt, F. Scholz, Electrochemical dictionary, Springer-Verlag, 2008.

[50] M. Bernt, H. A. H. Gasteiger, Influence of Ionomer Content in IrO 2 /TiO 2 Electrodes on PEM Water Electrolyzer Performance, Journal of The Electrochemical Society 163 (11) (2016) F3179–F3189. doi:10.1149/2.0231611jes.
URL http://jes.ecsdl.org/lookup/doi/10.1149/2.0231611jes

[51] J. Bockris, Z. Nagy, Symmetry Factor and Transfer Coefficient, Journal of Chemical Education.

[52] M. Noel, K. Vasu, Charge Tranfer Kinetics and Diffusion, in: Cyclic Voltammetry and the Frontiers of Electrochemistry, Oxford & IBH Publishing Co. Pvt. Ltd., New Delhi, 1990, pp. 157–194.
URL http://noel-cyclic-voltametric-one.tripod.com/cvm/Chapter-4.PDF

[53] R. Guidelli, R. G. Compton, J. M. Feliu, E. Gileadi, J. Lipkowski, W. Schmickler, S. Trasatti, Defining the transfer coefficient in electrochemistry: An assessment (IUPAC Technical Report), Pure and Applied Chemistry 86 (2) (2014) 245–258. doi:10.1515/pac-2014-5026.
URL http://www.degruyter.com/view/j/pac.2014.86.issue-2/pac-2014-5026/pac-2014-5026.xml

[54] J. M. Hu, J. Q. Zhang, C. N. Cao, Oxygen evolution reaction on IrO2-based DSA?? type electrodes: Kinetics analysis of Tafel lines and EIS, International Journal of Hydrogen Energy 29 (8) (2004) 791–797. doi:10.1016/j.ijhydene.2003.09.007.

[55] E. Slavcheva, I. Radev, S. Bliznakov, G. Topalov, P. Andreev, E. Budevski, Sputtered iridium oxide films as electrocatalysts for water splitting via PEM electrolysis, Electrochimica Acta 52 (12) (2007) 3889–3894. doi:10.1016/j.electacta.2006.11.005.

[56] U. Babic, M. Suermann, F. N. Büchi, L. Gubler, T. J. Schmidt, Critical ReviewIdentifying Critical Gaps for Polymer Electrolyte Water Electrolysis Development, Journal of The Electrochemical Society 164 (4) (2017) F387–F399. doi:10.1149/2.1441704jes.
URL http://jes.ecsdl.org/lookup/doi/10.1149/2.1441704jes

[57] M. V. Williams, H. R. Kunz, J. M. Fenton, Analysis of Polarization Curves to Evaluate Polarization Sources in Hydrogen/Air PEM Fuel Cells, Journal of The Electrochemical Society 152 (3) (2005) A635. doi:10.1149/1.1860034.

[58] K. C. Neyerlin, W. Gu, J. Jorne, H. A. Gasteiger, Determination of Catalyst Unique Parameters for the Oxygen Reduction Reaction in a PEMFC, Journal of The Electrochemical Society 153 (10) (2006) A1955. doi:10.1149/1.2266294.
URL http://jes.ecsdl.org/cgi/doi/10.1149/1.2266294